

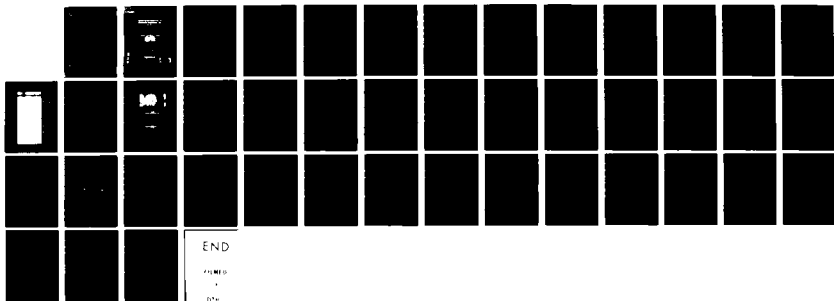
AD-A120 562

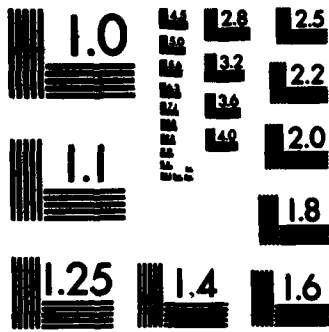
CHARGED PARTICLE DISTRIBUTIONS AND ELECTRIC FIELD
MEASUREMENTS TAKEN BY S. (U) AEROSPACE CORP EL SEGUNDO
CA SPACE SCIENCES LAB P F MIZERA ET AL. 01 OCT 82
TR-0083(3940-05)-1 SD-TR-82-71 F/G 20/7

1/1

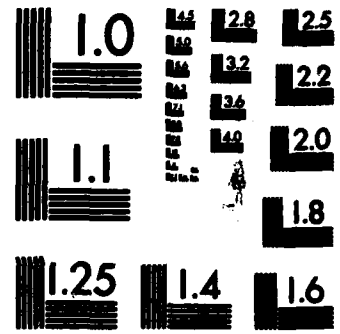
UNCLASSIFIED

NL

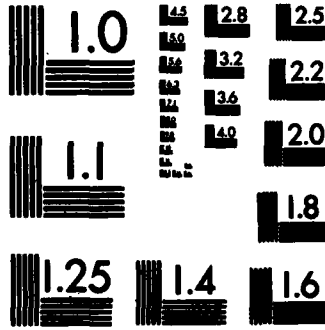




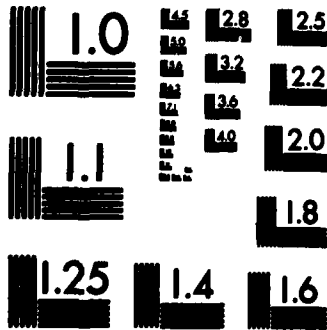
MICROCOPY RESOLUTION TEST CHART
NATIONAL BUREAU OF STANDARDS-1963-A



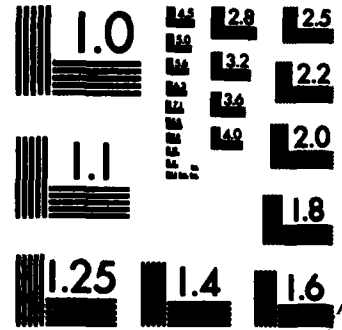
MICROCOPY RESOLUTION TEST CHART
NATIONAL BUREAU OF STANDARDS-1963-A



MICROCOPY RESOLUTION TEST CHART
NATIONAL BUREAU OF STANDARDS-1963-A



MICROCOPY RESOLUTION TEST CHART
NATIONAL BUREAU OF STANDARDS-1963-A



MICROCOPY RESOLUTION TEST CHART
NATIONAL BUREAU OF STANDARDS-1963-A

AD A120562

plates. All DTIC reproductions will be in black and white.

A

Prepared for
SPACE DIVISION
AIR FORCE SYSTEMS COMMAND
Los Angeles Air Force Station
P.O. Box 92960, Worldway Postal Center
Los Angeles, Calif. 90009

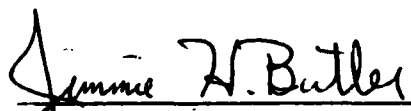
82 10 21 003

This report was submitted by The Aerospace Corporation, El Segundo, CA 90245, under Contract No. F04701-81-C-0082 with the Space Division, Deputy for Technology, P.O. Box 92960, Worldway Postal Center, Los Angeles, CA 90009. It was reviewed and approved for The Aerospace Corporation by H. R. Ruge, Director, Space Sciences Laboratory. Lt Randall S. Weidenheimer, SD/YLVS, was the project officer for the Mission-Oriented Investigation and Experimentation (MOIE) Program.

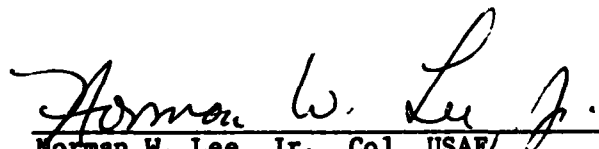
This report has been reviewed by the Public Affairs Office (PAS) and is releasable to the National Technical Information Service (NTIS). At NTIS, it will be available to the general public, including foreign nations.

This technical report has been reviewed and is approved for publication. Publication of this report does not constitute Air Force approval of the report's findings or conclusions. It is published only for the exchange and stimulation of ideas.


Randall S. Weidenheimer, 2nd Lt, USAF
Project Officer


Jimmie H. Butler, Colonel, USAF
Director of Space Systems Technology

FOR THE COMMANDER


Norman W. Lee, Jr., Col, USAF
Deputy for Technology

UNCLASSIFIED

SECURITY CLASSIFICATION OF THIS PAGE (When Data Entered)

REPORT DOCUMENTATION PAGE		READ INSTRUCTIONS BEFORE COMPLETING FORM
1. REPORT NUMBER SD-TR-82-71	2. GOVT ACCESSION NO. AD-A120562	3. RECIPIENT'S CATALOG NUMBER
4. TITLE (and Subtitle) CHARGED PARTICLE DISTRIBUTIONS AND ELECTRIC FIELD MEASUREMENTS TAKEN BY S3-3	5. TYPE OF REPORT & PERIOD COVERED	
	6. PERFORMING ORG. REPORT NUMBER TR-0083(3940-05)-1	
7. AUTHOR(s) Paul F. Mizera, Joseph F. Fennell, Donald R. Croley, Jr., and David J. Gorney	8. CONTRACT OR GRANT NUMBER(s) F04701-82-C-0083	
	10. PROGRAM ELEMENT, PROJECT, TASK AREA & WORK UNIT NUMBERS	
9. PERFORMING ORGANIZATION NAME AND ADDRESS The Aerospace Corporation El Segundo, Calif. 90245	12. REPORT DATE 1 October 1982	
	13. NUMBER OF PAGES 37	
11. CONTROLLING OFFICE NAME AND ADDRESS Space Division Air Force Systems Command Los Angeles, Calif. 90009	15. SECURITY CLASS. (of this report) Unclassified	
	15a. DECLASSIFICATION/DOWNGRADING SCHEDULE	
16. DISTRIBUTION STATEMENT (of this Report) Approved for public release; distribution unlimited		
17. DISTRIBUTION STATEMENT (of the abstract entered in Block 20, if different from Report)		
18. SUPPLEMENTARY NOTES		
19. KEY WORDS (Continue on reverse side if necessary and identify by block number) Auroral arcs Electrostatic shocks Inverted "V" structures Ion beams Ion conics		
20. ABSTRACT (Continue on reverse side if necessary and identify by block number) → Comparisons of electron and proton distribution functions are made with DC electric field measurements as the S3-3 satellite crossed a series of high latitude acceleration regions near local dusk on July 29, 1976. Potential drops from parallel electric fields are inferred from charged particle distributions using adiabatic theory and compared with potentials calculated from measured perpendicular electric fields. There exists a one-to-one spatial relationship between strong DC electric field enhancements in the form		

UNCLASSIFIED

SECURITY CLASSIFICATION OF THIS PAGE(When Data Entered)

19. KEY WORDS (Continued)

20. ABSTRACT (Continued)

of electric field reversals and acceleration signatures of auroral particles. From the charged particle and electric field analysis, we conclude that electric fields, parallel to B_z , can extend above and below the satellite altitude near 7500 km when strong electrostatic field reversals are encountered. Within the uncertainties of our analysis, the potential drop below the satellite is comparable to the potential calculated from the individual electrostatic structures crossed by the satellite. There are, in addition, particle signatures that imply a source of strong acceleration was located above and relatively close to the satellite. These accelerated electrons are coincident with auroral hiss and ion conics. In addition to regions of acceleration that extended only fractions of a degree in latitude, there was a broad "inverted V structure" near the polar cap boundary where strong perpendicular electric fields were embedded, giving rise to large variations in the inferred potential below the satellite.

UNCLASSIFIED

SECURITY CLASSIFICATION OF THIS PAGE(When Data Entered)

PREFACE

The DC electric field measurements were provided by the Space Sciences Laboratory at the University of California at Berkeley. Dr. R. Torbert was especially helpful in producing the processed data. Dr. R. Sharp of the Lockheed Research Laboratory kindly furnished ion measurements.



Author	
Title	
Source	
Availability Codes	
Avail and/or Special	

A

CONTENTS

PREFACE..... 1

INTRODUCTION..... 7

INSTRUMENT AND DATA DESCRIPTION..... 9

PRESENTATION OF RESULTS..... 15

DISCUSSION..... 37

REFERENCES..... 39

FIGURES

1.	Colored Spectrogram of AC Electric Fields, Energetic 235 keV Electrons, 0.14 to 33 keV Electrons, 0.90 to 3.9 keV Ions and Energetic 80 keV Protons for July 29, 1976.....	11
2.	The Low Energy Charged Particles from Fig. 1 are Aligned in Time With the Perpendicular Component of the Electric Field Measured by the UC Berkeley Experiment.....	13
3.	Charged Particle Distribution Contours for the First Electrostatic Shock Encounter.....	18
4.	The Second Narrow Shock Encounter as Exemplified by Charged Particle Distribution Functions.....	21
5.	The Third of the Four Shock Crossings as Shown by Charged Particle Distribution Functions in Velocity Space.....	24
6.	The Last Encounter With a Narrow Electrostatic Shock is Described by the Charged Particle Velocity Space Distribution Functions.....	26
7.	Ion and Electron Phase Space Density Contours for a Region Where the Inferred Potential Above the Satellite is Near 9 kV and the Potential Below the Satellite is of the Order of 100 Volts.....	27
8.	Distribution Function of Ions (Protons) and Electrons for a Highly Accelerated Electron Population and Accompanying Ion Conics.....	28
9.	Ion Phase Space Density Contours in Fig. 9a Showing the Crossing of an Ion Conical Distribution Outside of the Ionospheric Loss Cone.....	31

TABLE

1. **Times, Peak Energy, and Intensity of Proton Beams Estimated from Data Taken by the Electrostatic Analyzer with Energies from 0.09 to 3.9 keV and the Ion Compositions Spectrometer with Energies Between 0.5 to 16 keV..... | 33**

INTRODUCTION

Particle and field measurements, taken by the USAF S3-3 satellite, have been recognized by the scientific community as providing important information for the description and understanding of the auroral acceleration process. Ion composition analyses have revealed that a major source of positive charged particle density in the magnetosphere originates in the auroral oval (Shelley et al., 1976) and consists of the major ionospheric species of H^+ , He^+ and O^+ . Two categories of ion distributions are observed, ion beams along B and ion conics whose peak intensity occurs between 90° and 180° pitch angle in the northern hemisphere (Mizera and Fennell, 1977 and Sharp et al., 1977). One of the most dramatic aspects of the S3-3 observations has been the measurement of strong DC electric fields perpendicular to B (Mozer et al., 1977; Torbert and Mozer, 1978). AC electric field measurements have also provided excellent correlations between particles and ion cyclotron waves (Kintner et al., 1979), as well as a description of low frequency turbulence (Temerin, 1978). Electron distributions have been utilized to infer large spatial extensions of parallel DC electric fields (Mizera and Fennell, 1977; Sharp et al., 1979). Techniques developed to infer these potentials have been discussed previously by Whipple, 1977; Chiu and Schulz, 1978; Croley et al., 1978; and Cladis and Sharp, 1979.

Most of the above references pertain to individual examples of S3-3 acquisitions. There have also been statistical studies by Ghielmetti et al., 1978 and Gorney et al., 1980) on the frequency of occurrence of ion beams from the ionosphere. This type of study has been expanded to include field aligned current systems and electrostatic shocks by Cattell et al., 1979.

For almost historical reasons, data for both particles and fields taken on July 29, 1976 have been widely publicized. Other data previously published from this event include Mozer et al., 1977; Sharp et al., 1979; Cornwall and Schulz, 1979; and Chiu and Cornwall, 1979. Their results will be included as we describe this auroral crossing in detail. Perhaps one of the most spectacular results from this data was the first observation of large DC electric fields associated with this altitude region (Mozer et al., 1977). A summary of their data with a charged particle spectrogram was presented in Cornwall and Schulz, 1979, as Figs. 2 and 3. Association of ion beams and accelerated electron distributions with these electric field reversals was presented by Mizera et al., 1977. Sharp et al., 1979, examined individual electron distributions to infer characteristics of the acceleration process. We wish to add one more and final contribution by presenting the total data set of individual encounters of plasmas with acceleration signatures in the form of electrostatic shocks, ion beams, ion conics and electron distributions. AC electric field intensity enhancements in the form of broadband signals are also shown to co-exist with certain individual structures.

Instrumentation and Data Description

A complete description of the S3-3 experimental techniques can be found in Mizera et al., 1979. Individual descriptions of electric field instrumentation were presented in Mozar et al., 1977, of ion composition instrumentation in Sharp et al., 1977, and of low energy electrons and ion instrumentation in Mizera and Fennell, 1977. The particle spectrogram display (Figures 1 and 2) is derived from data taken by two electrostatic analyzers and an energetic magnetic spectrometer and an ion telescope. Filter outputs of the AC electric field experiment are tape recorded along with the particle measurements. High resolution electric field data are also transmitted in real time on a limited basis. The July 29, 1976 data were acquired when apogee (near 8000 km) was over the northern auroral region near dusk.

Standard energy-time spectrogram formats are used with differential energy flux of electrons and ions. The intensity scales for the 235 keV electrons and 80 keV protons are arbitrary. AC electric field data are presented in units of $\mu\text{volts}/(\text{m Hz}^{1/2})$. Velocity-space distribution functions are derived from particle distributions of electrons from 0.17 to 33 keV and ions from 0.90 to 3.9 keV.

Fig. 1. Spectrogram of AC Electric Fields, Energetic 235 keV Electrons, 0.17 to 33 keV Electrons, 0.90 to 3.9 keV Ions and Energetic 80 keV Protons for July 29, 1976. Five orders of magnitude in dynamic range of intensities can be distinguished. The arrows at the top indicate the location of electrostatic field reversals, accelerated electrons, and ion beams.

(following page)

S3-3 JULY 29, 1976

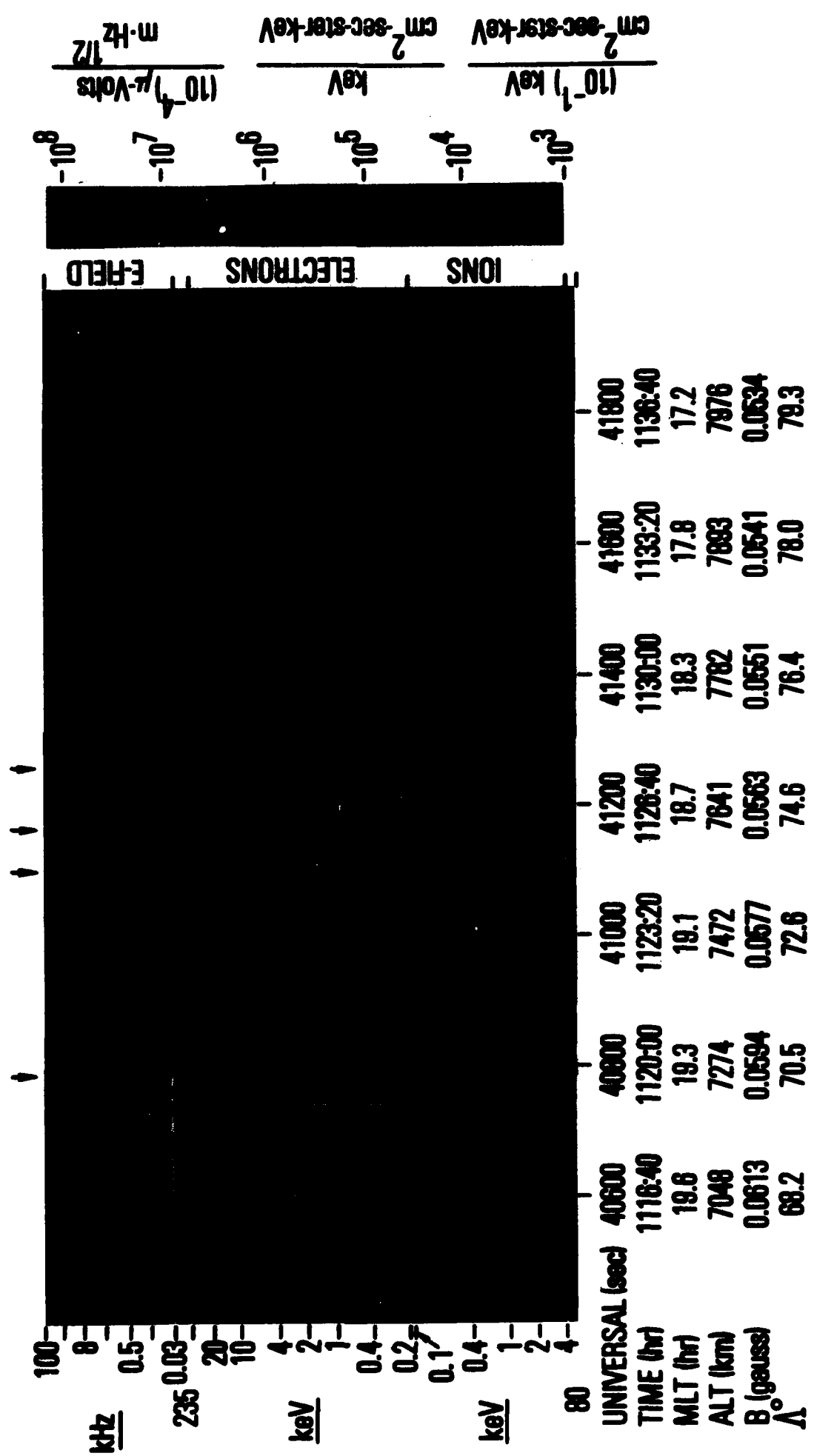
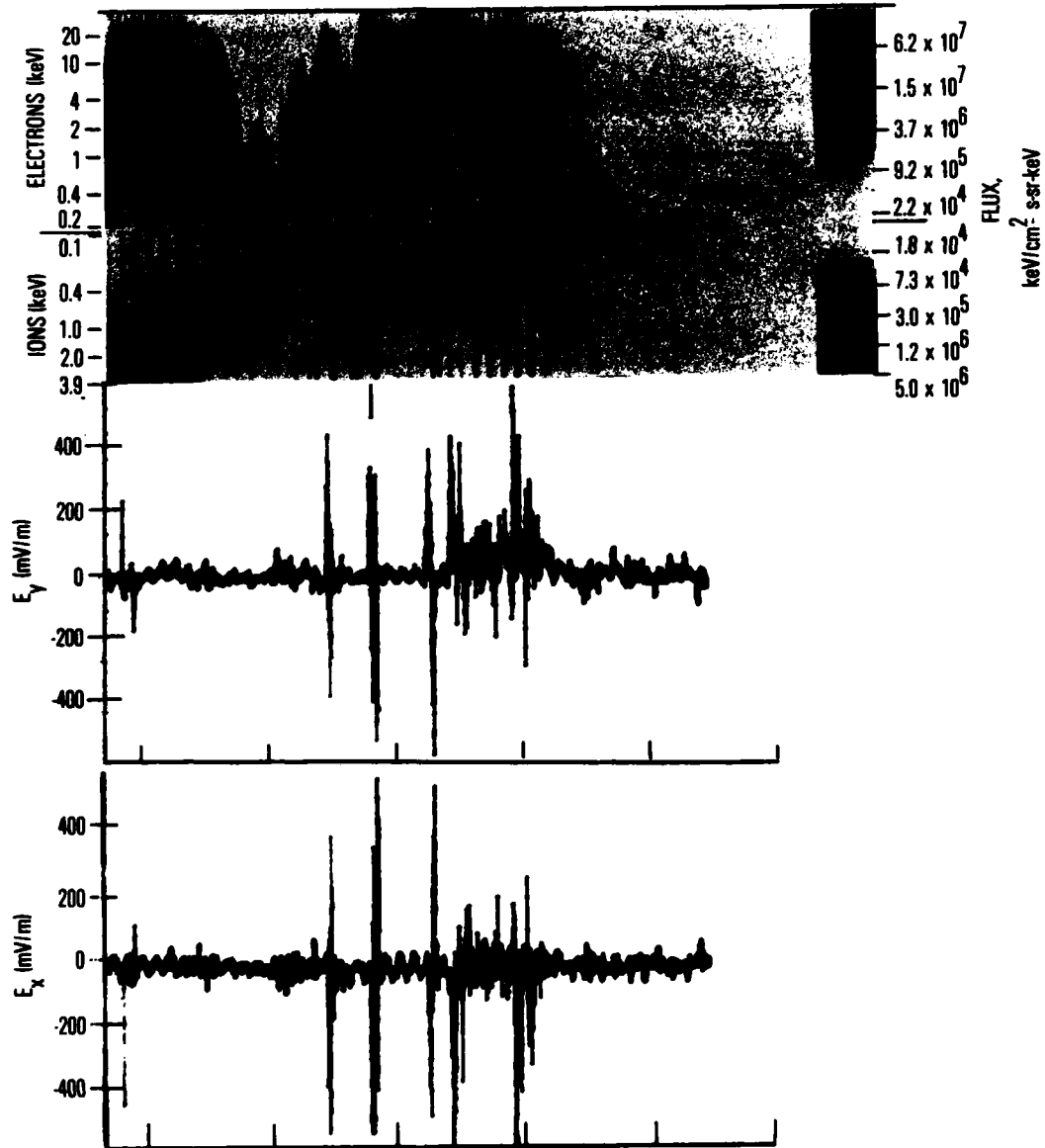


Fig. 2. The Low Energy Charged Particles from Fig. 1 are Aligned in Time with the Perpendicular Component of the Electric Field Measured by the UC Berkeley Experiment (R. Torbert, private communication, 1978)

(following page)

S3-3

JULY 29, 1976



UT, (sec)	40800	41000	41200	41400	41600
INV LAT	70.5°	72.6°	74.6°	76.4°	78.0°
MAG LT	19.3°	19.1°	18.7°	18.3°	17.8°
ALT, km	7274	7472	7641	7782	7893
B , γ	5840	5770	5630	5510	5410

Presentation of Results

Dusk auroral measurements, taken by S3-3 on July 29, 1976, have been shown in fragmented parts by various authors. For this reason and the fact that a great diversity of observations are present, we will present as complete a description of this single auroral acquisition as possible.

Fig. 1 shows our standard energy-time spectrogram that contains AC electric field measurements from the UC Berkeley experiment with frequencies ranging from ~ 30 Hz to ~ 100 kHz in units of $(10^{-4} \text{ } \mu\text{volts/m-Hz}^{1/2})$. These data are broad resolution measurements taken with filters and should be interpreted only as indicating the true wave spectrum. Particle measurements include energy fluxes from an electron and an ion electrostatic analyzer with energies ranging from ~ 0.17 to 8.4 keV and 0.09 to 3.9 keV, respectively. Electrons up to 33 keV are included in the spectrogram with absolute normalization.

Differential fluxes (with arbitrary values) are shown for 235 keV electrons and 80 keV protons in Fig. 1 for purposes of displaying energetic particle boundaries. Ephemeris parameters as well as universal times are calculated every 200 seconds at the bottom. At this time, S3-3 was making a complete angular rotation every 23 seconds and thus angular distributions were acquired every 11.5 seconds. The periodic minima in the particle intensities represent pitch angle sweeps through the magnetic field.

As S3-3 approached the energetic trapping boundary located near $\Lambda \sim 70.5^\circ$ and 19.3 . MLT, the low altitude near-earth plasma sheet is evident by the gradual hardening of the electron energy flux beginning near 40480 sec UT in Fig. 1. A number of narrow regions of particle accelerations were

encountered before S3-3 entered the polar cap near 41500 sec UT. These narrow acceleration regions are shown by arrows in Fig. 1, and we will examine each one individually by presenting particle distribution functions with empirically determined potential boundaries. This procedure has been adequately described in previous publications, including Whipple, 1977; Mizera and Fennell, 1977; Chiu and Schulz, 1978; and Croley et al., 1978.

A natural question that immediately arises is whether the potential drop, measured at the S3-3 altitude by integrating the electric field perpendicular to \underline{B} , is related to the potential difference inferred from particle distributions in a way described by Mizera and Fennell, 1977, and Cladis and Sharp, 1979. In an attempt to answer this question, the composite particle-DC electric field display, first used in Cornwall and Schulz, 1979, is shown as Figure 2 to identify regions of interest. The \mathcal{E}_y (east-west) perpendicular component was chosen just to illustrate the location of shocks; normally \mathcal{E}_x is used (Torbert and Mozar, 1978).

The first encounter with strongly accelerated particle fluxes and large DC electric field occurs near 40769 sec UT (40.77 ksec). The \mathcal{E}_y electric field component was positive, indicating a westward direction, and the \mathcal{E}_x component was negative, indicating a northward direction, of the perpendicular electric field. Low-frequency turbulence (< 500 Hz) was associated with this encounter until the oppositely directed perpendicular fields were measured near 40787 sec UT. Near 40769 sec UT, the \mathcal{E}_x and \mathcal{E}_y magnitudes were approximately -480 mV/m and $+240$ mV/m, giving a total electric field, perpendicular to \underline{B} , of ~ 537 mV/m pointing in a northwesterly direction. To estimate the potential drop perpendicular to \underline{B} , we ask over what distance the field was observed and integrate the electric field along the trajectory of the satellite. The results of the electric field calculations were provided by the U C

Berkeley group. The calculation assumes time-stationary electric field structures (R. B. Torbert, private communication, 1979).

i.e.,
$$\Delta t (\underline{v} \cdot \underline{E}) = \Delta \phi (\text{kV}) \quad (1)$$

where v is the velocity of the satellite and \underline{E} is the total perpendicular electric field. If we estimate the potential below the satellite using particle distribution functions, then we can compare the results of these two procedures. This, of course, assumes that the equipotentials crossed near 7300 km altitude are approximately the same as those crossed by the upcoming ion beam and downgoing electrons near 40.77 ksec UT.

Fig. 3 shows proton and electron distribution functions for (a) 40778 to 40789 sec UT and (b) 40784 to 40795 sec UT. Although the ion beam can only be observed when the instrument points in the nadir hemisphere along \underline{B} , the acceleration region is evident in Fig. 1 over all pitch angles where low energy backscattered electrons are retarded by the potential below. For example, in Fig. 1, the decrease in fluxes of electrons with energies below ~ 0.5 keV is apparent near 40769 sec UT and is caused by a shift in energy in the secondary electron spectra due to a retarding potential between the satellite and the ionosphere. This characteristic feature in the spectrogram allows the correlation between particles and fields to be made with higher spatial resolution.

Fig. 3 also shows boundaries that separate phase space density regions. These regions are determined by examining adiabatic motion of particles in quasi-static electric fields and the techniques employed to determine them have been widely discussed (Whipple, 1977; Chiu and Schulz, 1978; Kaufmann, 1978; Mizera and Fennell, 1977; and Croley et al., 1978). The energy at the

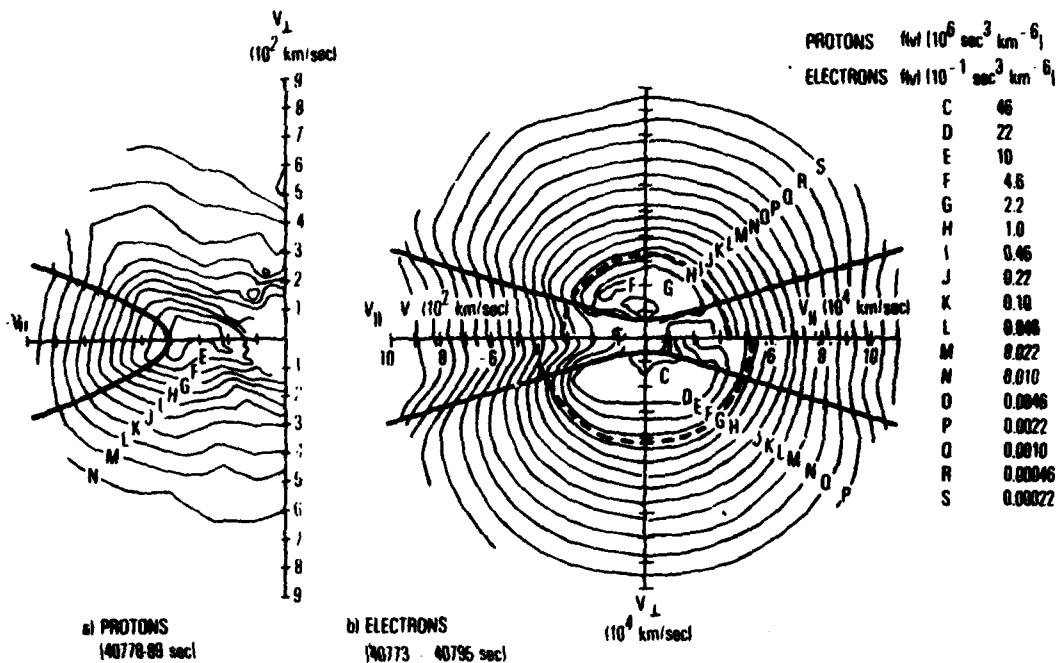


Fig. 3. Charged Particle Distribution Contours for the First Electrostatic Shock Encounter. Figure 3a shows the counter-clockwise satellite rotation through the nadir that contains an ion beam whose peak energy occurs near 0.8 keV ($v_p \approx 390$ km/sec). The solid line is a hyperbola in velocity space calculated assuming adiabatic motion in a quasi-static electric field whose potential drop below the satellite is ≈ 0.8 kV. Figure 3b shows the satellite rotation in the counter-clockwise direction starting at $+v$ and measuring electrons with pitch angles from 0° to 360° . In addition to the solid line which represents a hyperbola derived from the same approximations as those used in Fig. 3a, the dashed line represents an ellipse whose intercepts were derived from adiabatic motion of particles having been accelerated by a ~ 5 kV potential above the point of observation. Phase space densities are shown as contours marked by letters with the appropriate scaling factors. Electrons with velocities inside the ellipse have not participated in the full acceleration. Electrons between the v axis and the hyperbola are assumed to have originated from the ionosphere in both hemispheres. Electrons between the hyperbola and the ellipse are electrostatically trapped.

peak of the intensity of the upcoming ion spectrum is used to calculate the hyperbola intercept along the v_{\perp} axis in Fig. 3a. The potential above the satellite is relatively easy to estimate, from the electron spectrum. This value is used to estimate the location of the ellipse in Fig. 3b. There is a well-defined peak in the precipitating electron spectrum near ~ 5 keV at small pitch angles. This corresponds to an ellipse which intercepts $v_{\perp} = 4.2 \times 10^4$ km/sec in Fig. 3b. The potential below the satellite is more difficult to estimate and we rely on the peak energy of the ion beam to provide a minimum potential estimate. That is, ions can originate at altitudes higher than the termination of the electric field down to the ionosphere. This, of course, assumes that most of the ion kinetic energy is due to a static DC electric field acceleration along \underline{B} and ignores perpendicular heating (Lysak et al., 1979; Unstrup et al., 1979).

The solid line in Fig. 3a corresponds to the demarcation boundary between ionospheric and magnetospheric densities whose velocity along $-v_{\perp}$ is ~ 400 km/sec and corresponds to a proton energy of ~ 0.8 keV. For the sake of comparison, we take the potential below the satellite to correspond to the peak of the ion beam energy (~ 0.8 keV) and use this as the minimum retarding potential boundary for electrons. This energy corresponds to an electron velocity of $v_{\perp} = 0.57 \times 10^4$ km/sec and provides the intercept for the hyperbola in Fig. 3b. In Fig. 3b, phase space densities (C, D, E, and F) along $0.6 < v_{\perp} < 4.2 \times 10^4$ km/sec are in the trapping region between magnetic mirror points below and the electrostatic reflection above the satellite altitude. From the ordering of phase-space density contours between the intersection of the ellipse and the hyperbola in Fig. 3b, 0.8 kV is reasonable to represent the potential drop below the satellite. Using Eq. 1, the calculated potential drop near ~ 40768 sec UT is approximately 1 kV. Under these assumptions, the

integrated electric field and the potential below inferred from particle distributions are equal.

The next example of DC electric field reversals associated with ion beams and accelerated electron distributions occurs near 41090 sec UT and is indicated by the second arrow in Fig. 1. For this case, the electric field signal showed some evidence of saturation effects and Eq. 1 can be used only to estimate the lower limit of the potential; however, the signal was not strongly saturated. Figure 4b shows electron velocity contours of the distribution function for 41096 to 41107 sec UT. The strong electric field signals occurred between 41087 and 41091 sec UT, with the lower-latitude field again pointing in a northwesterly direction with a maximum intensity near 580 mV/m. The reversal to a southeasterly direction was recorded between ~ 41093 to 41095 sec UT. Fig. 4b shows one estimate of the potential above the satellite altitude of 7560 km to be approximately 5 kV. The dashed circle near 4.1×10^4 km/sec is the demarcation between phase-space densities of electrons above and below this velocity. Fig. 4a shows ion (proton) distribution functions for ~ 41089 to 41101 sec UT. The maximum energy of the upcoming ion beam is near 2.3 keV, and this results in a hyperbola that intersects the $-v_x$ axis near 660 km/sec. Ions contained in this beam have been accelerated by a potential near 2 kV below the satellite. As previously indicated in Fig. 3a, a lower velocity intercept is needed in order to contain all of the contours of accelerated ions. This may mean that the ions experience a dispersion in energy over some altitude range or we should change our assumption that the ions are not totally hydrogen. The latter effect would modify the distribution functions by a factor of $[m_1/m_H]$ and the velocity by a factor of $(m_H/m_1)^{1/2}$. Regardless of these assumptions the total acceleration is independent of ion species, as long as we rule out multi-charged ions such as H_e^{++} and O^{++} originating from low altitudes.

PROTONS	$f(v) (10^6 \text{ sec}^{-3} \text{ km}^{-3})$	b_j
C	46	
D	27	
E	10	
F	4.6	
G	2.2	
H	1.0	
I	0.46	
J	0.22	
K	0.10	
L	0.046	
M	0.022	
N	0.010	
O	0.0046	
P	0.0022	
Q	0.0010	
R	0.00046	
S	0.00022	

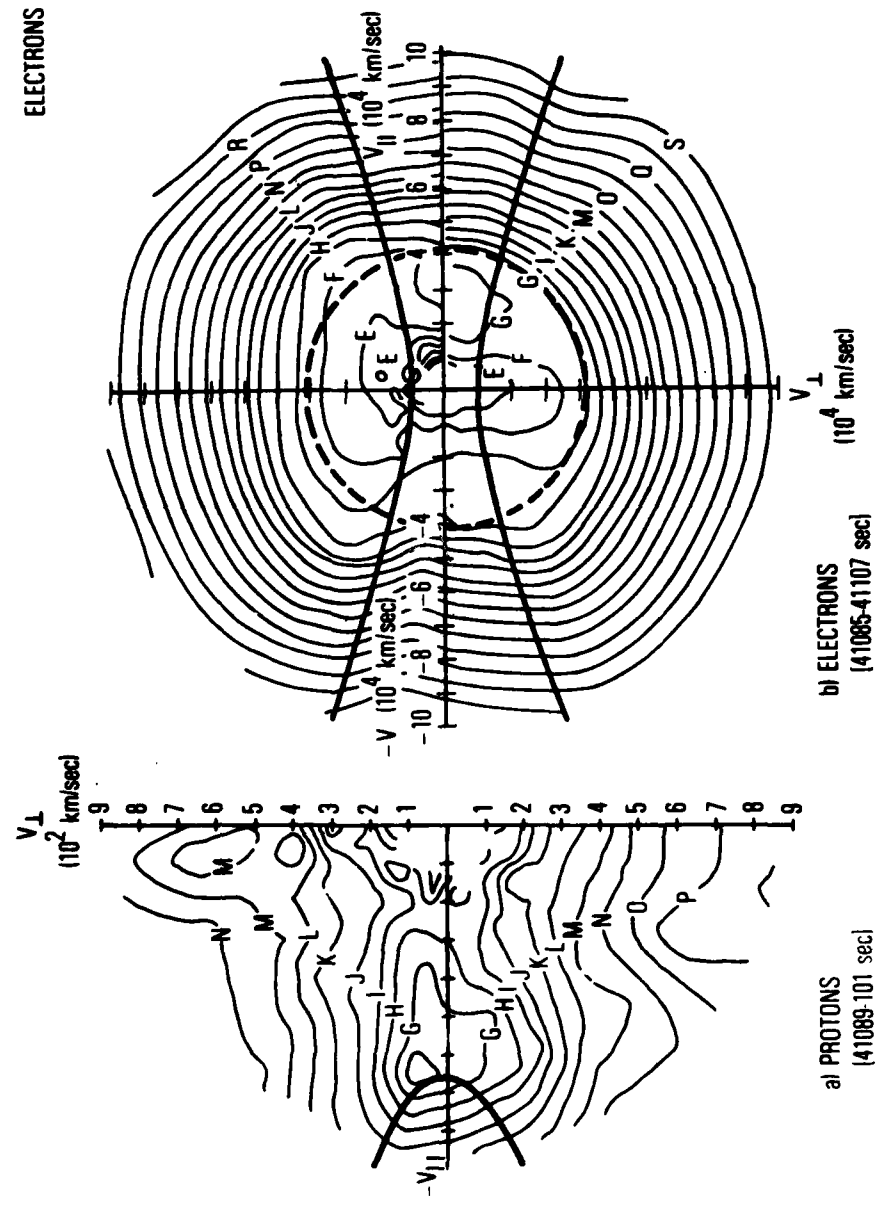


Fig. 4. The Second Narrow Shock Encounter as Exemplified by Charged Particle Distribution Functions. Figure 4a shows a broad ion beam with a maximum energy near 2.5 keV. Figure 4b shows electron phase space densities after acceleration by approximately 5 kv above the satellite. The solid and dashed curves are explained in Fig. 3.

If we take a lower limit of the potential to be ~ 2.3 kV, based on the peak energy of the ion beam spectrum, then a hyperbola that intersects the electron v_{\perp} axis near 0.72×10^4 km/sec is drawn in Fig. 4b. One might argue that a hyperbola shifted toward higher velocities would separate the phase space density boundaries in a more reasonable fashion. This would mean that the inferred electric field could extend down below the altitude from where the majority of ions originate. Using Eq. 1 to estimate the potential drop along the satellite trajectory, we obtain a value of ~ 4 kV. Our estimate from the particle distributions, using a low altitude potential of 2.3 kV or greater, is consistent with the calculated value using the perpendicular electric fields at satellite altitude. For the first two cases examined, the DC potential drop derived from Eq. 1 is comparable to the value inferred from upcoming ion beams and electron loss cone analysis. As was pointed out by Croley et al. 1978, the loss cone analysis of the electron distributions is not very sensitive in predicting the low altitude potential, because the ratio of low-altitude magnetic field intensity to that measured at the satellite is large (~ 10) and divides the velocity term.

The next example of electric field reversals and ion beams occurs with highly accelerated electrons. The electric field is less structured and is strongly saturated. Northwesternly perpendicular DC electric fields are encountered between ~ 41153 to 41158 sec UT, then some structured fields are measured from ~ 41159 to 41162 sec UT, and then the southeasterly component occurs between ~ 41164 to 41167 sec UT. A decrease of the secondary electron intensity, which signifies upward-directed electric fields along \underline{B} between the spacecraft and the atmosphere, begins near 41153 sec and ends near 41166 sec UT. The onset of strong \mathcal{E}_{\perp} signals and retarded secondary electrons is another excellent example of the correlation between the particles and

fields. Our best estimate of the saturated DC electric field between 41154 to 41157 sec UT yields a lower limit of ~ 590 mV/m.

Fig. 5b shows electron distribution functions for times 41151 to 41162 sec UT. The electron acceleration peak at the satellite altitude is approximately 8 keV, the result of which is shown by the dashed circle. Eq. 1 yields a potential drop across the northwesterly structure of ~ 8 kV and is only a lower limit due to saturation of the instrument. Without higher energy ion data (> 3.9 keV) we can not estimate the exact peak energy of the ion beam. However, from the electron distributions in Fig. 5b, a hyperbola corresponding to a low-altitude potential near 10 kV is in reasonable agreement with the data. Exiting the shock near 41164 sec UT, the electric field integration gives a potential drop closer to 5 kV. The hyperbola in Fig. 5a is a lower limit drawn for a potential near 3 kV.

The last electrostatic structure in this series occurs near 41242 sec UT, when \mathcal{E}_1 is again in a northwesterly direction with a maximum value near 600 mV/m. The reversal occurs between ~ 41252 to 41256 sec UT with a southeasterly direction whose maximum value is near 858 mV/m. Using the integration technique in Eq. 1, the UC Berkeley experiment gives a minimum potential drop along the satellite trajectory of ~ 7 kV, which is again a lower-limit estimate due to some saturation effects.

Fig. 6b shows the electron phase space density contours for a time interval 41240 - 41251 sec UT. The downgoing electron spectrum again peaks near 8 keV, as indicated by the ellipse intersecting the velocity axis near 5.3×10^4 km/sec, and demarcates the boundary between contours of accelerated fluxes above 8 keV and those below 8 keV. Fig. 6a clearly shows that the accompanying ion beam, encountered near 41251 sec UT, has a peak energy greater than 3.9 keV. Therefore, we rely solely on the electron distribution functions to

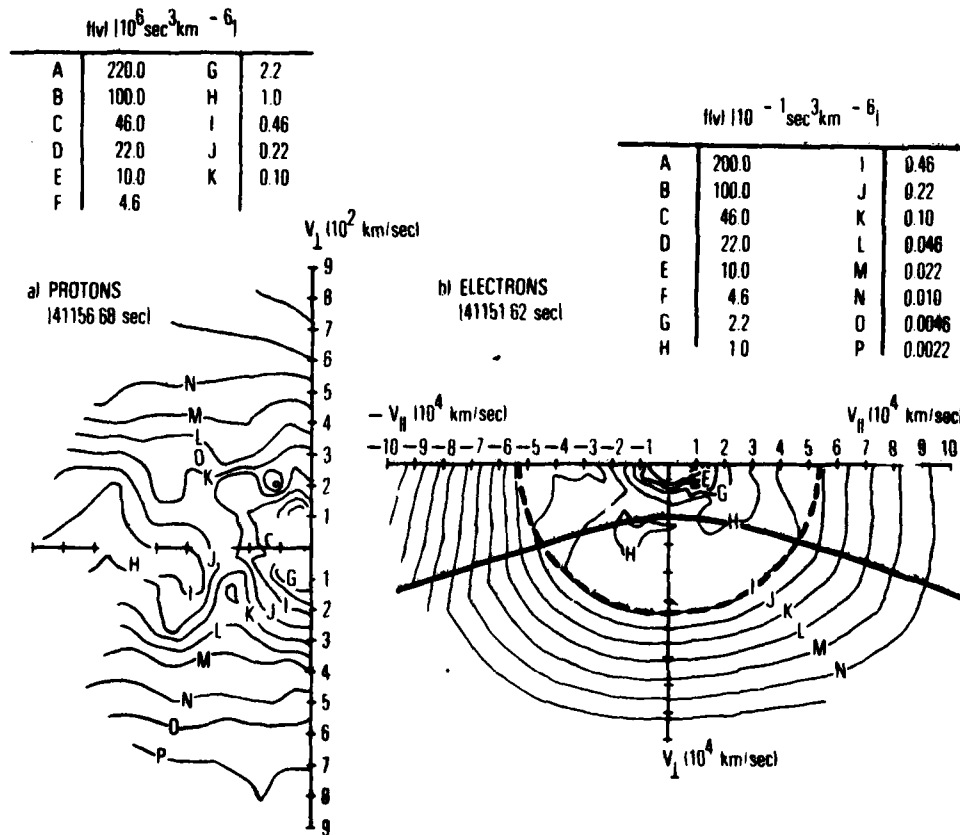


Fig. 5. The Third of the Four Shock Crossings as Shown by Charged Particle Distribution Functions in Velocity Space. Figure 5a shows a minimum potential estimate near 2.5 kV as shown by the intersection of the hyperbola and the v_{\parallel} axis near 660 km/sec. The estimate of the potential above the satellite is ≈ 8 kV as indicated by the dashed ellipse (circle) which intersects the $|v|$ axis near 5.4×10^4 km/sec.

estimate the magnitude of the potential below the satellite altitude. Using the calculated potential from Eq. 1 of ~ 7 kV, a hyperbola in velocity space is drawn in Fig. 6b to separate fluxes that mirror above the atmosphere from those originating in the atmospheric loss cone. Based on these empirical boundary fits to the electron distribution function, we infer the S3-3 satellite crossed an electrostatic structure with a potential of approximately equal magnitude above and below satellite altitude with a total drop near 15 - 16 kV.

To contrast this example with a region where the potential is primarily above the satellite altitude, we show an example from 41229 to 41240 (41.3 k) sec UT. An example of the electron angular distributions for this time period was given by Sharp et al., 1979, where they estimated the potential to be above S3-3 altitude with magnitudes in the 7-15 kV range. Fig. 7b shows distribution function contours for these electron data. The contours clearly indicate that the potential above the satellite altitude corresponds to an energy of $\sim 8-9$ keV ($v = 5.5 \times 10^4$ km/sec). Upcoming ions, shown in Fig. 7a show a hint of acceleration with potentials less than ~ 100 V. This estimate, also in agreement with electron loss-cone analysis, is represented as the hyperbola in Fig. 7b.

We now focus our attention on a slightly different aspect of the charged particle data. In the time interval from ~ 40900 to 40980 sec UT in Fig. 1, in between the first and second field reversal, highly anisotropic, accelerated electron distributions were encountered, accompanied by low-energy conical ion distributions (see Fig. 2 for a better definition). Based on our measurements, the peak energy in the precipitating electron spectrum is near 12 keV at UT = 40906 (40.9 k) sec UT. The shapes of the electron velocity space contours along the v_{\parallel} axis are distinctively different, as shown in Fig. 8b, when compared with previous examples. A circle (ellipse) is sketched as in

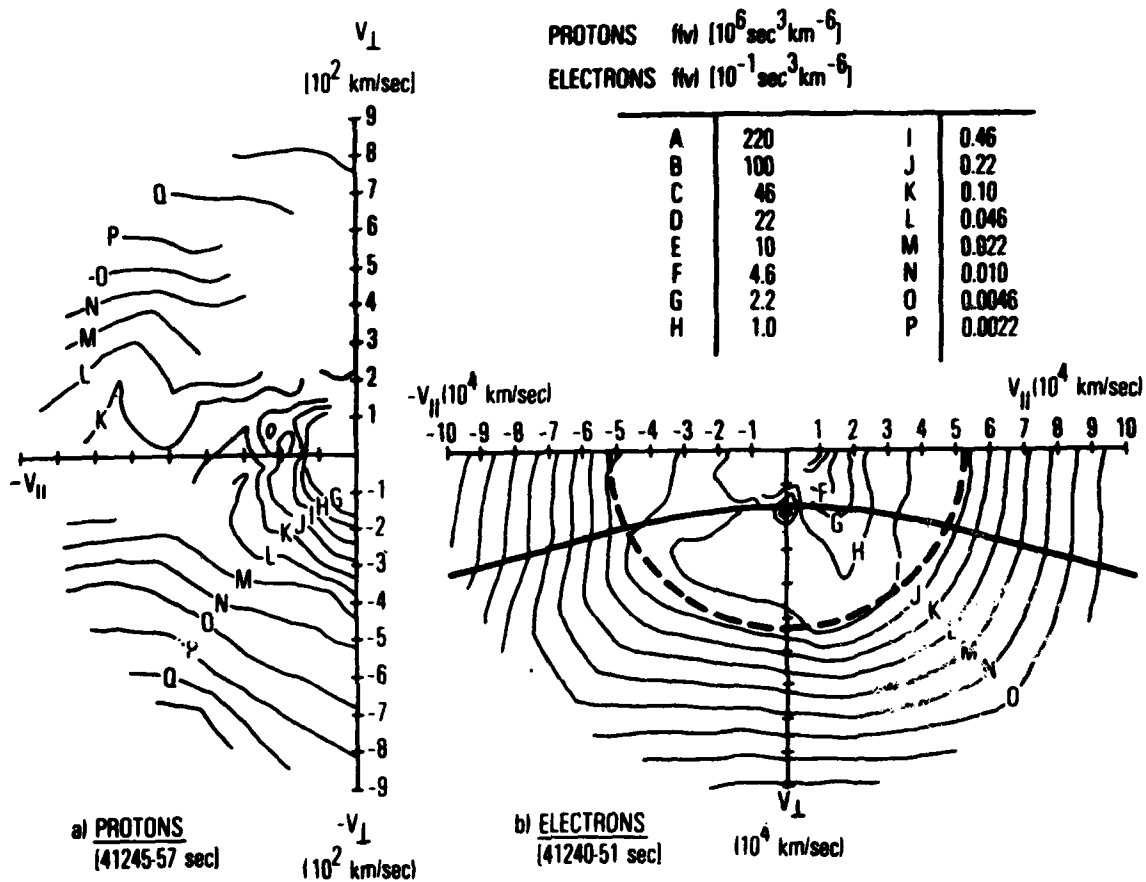


Fig. 6. The Last Encounter with a Narrow Electrostatic Shock is Described by the Charged Particle Velocity Space Distribution Functions. The ion beam in Fig. 6a has peak intensities above the 3.9 keV upper limit of the instrument. As was the case in Fig. 5b, an 8 kV potential is inferred from the precipitating electron spectrum and used to generate the dashed ellipse.

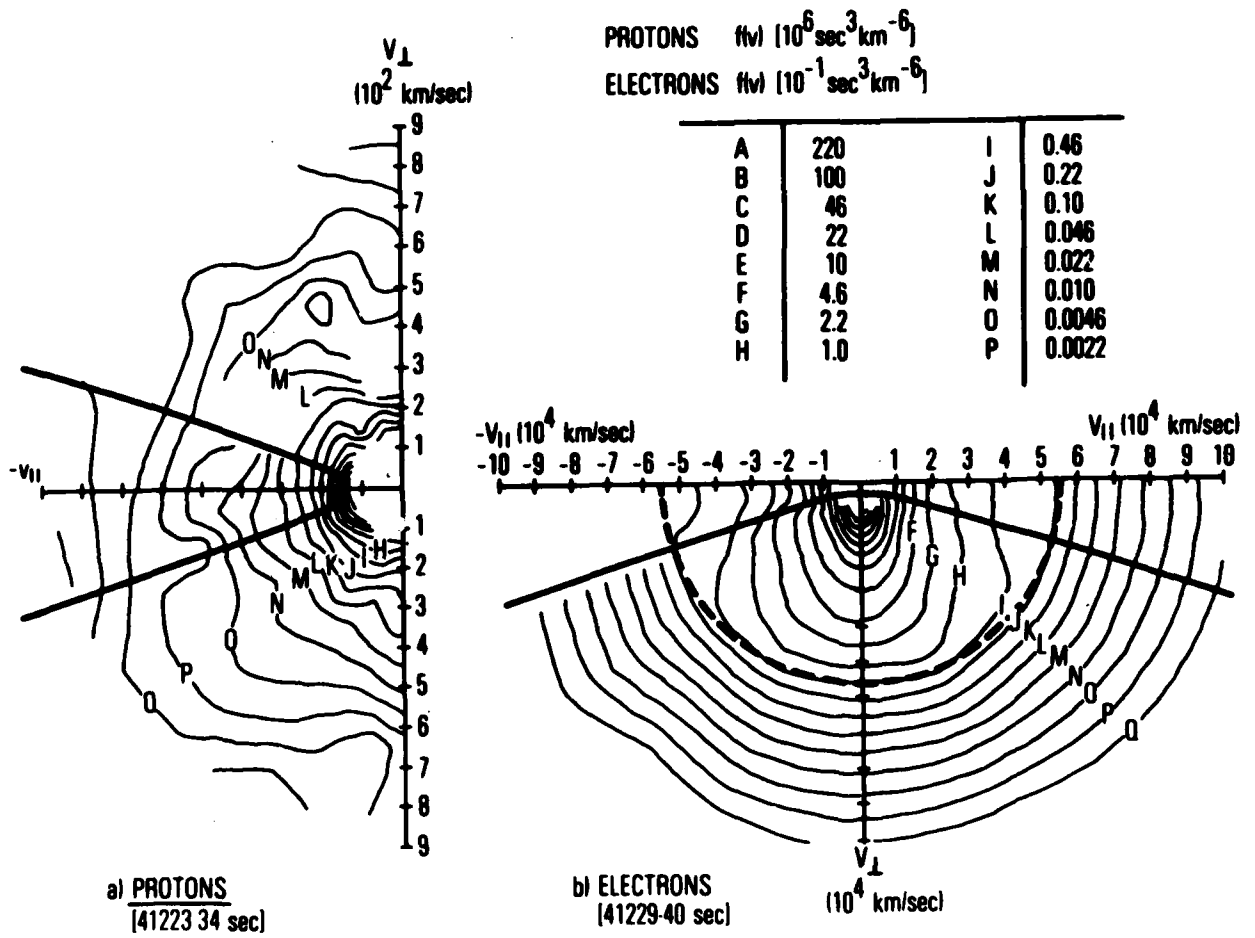


Fig. 7. Ion and Electron Phase Space Density Contours for a Region Where the Inferred Potential Above the Satellite is Near 9 kV (dashed ellipse) and the Potential Below the Satellite is of the Order of 100 Volts (solid hyperbola)

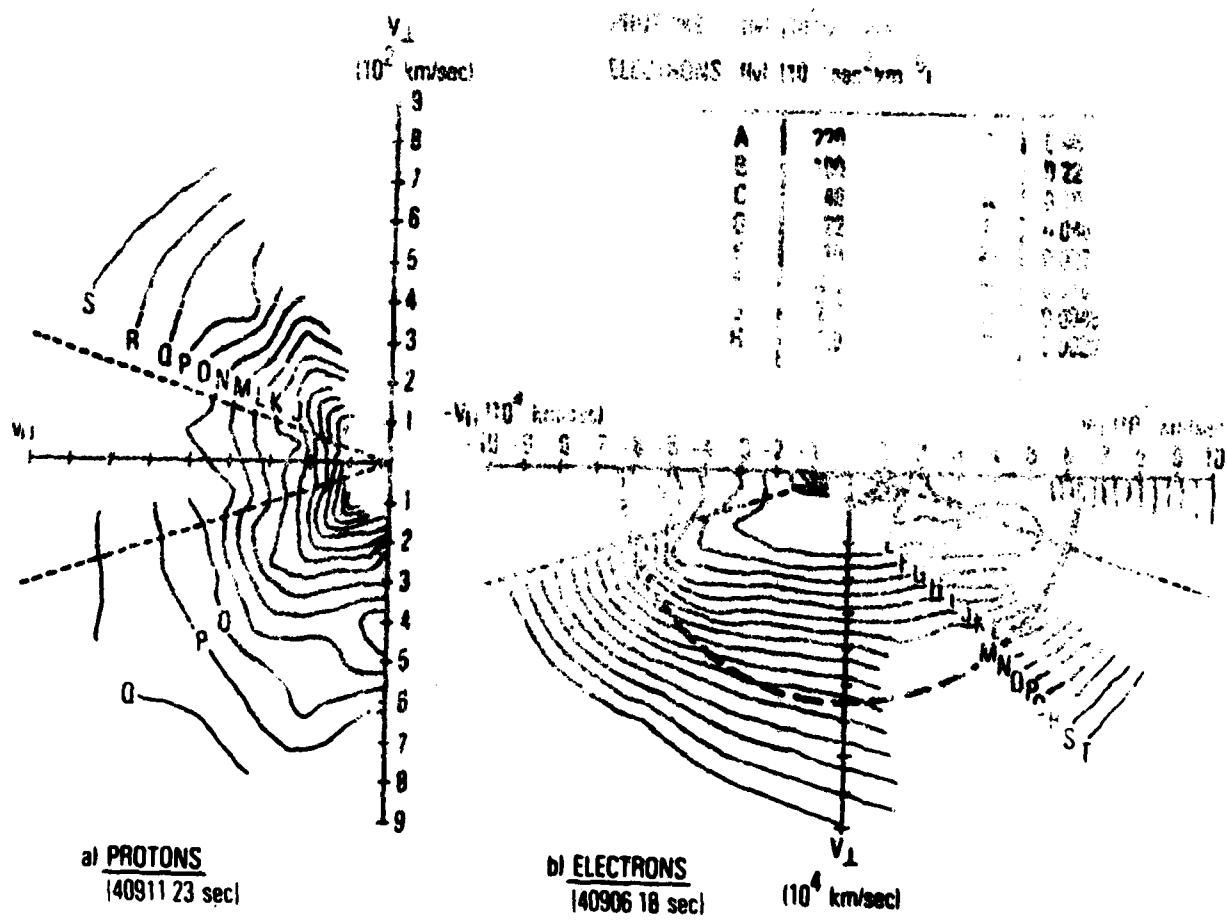


Fig. 8. Distribution Function of Ions (protons) and Electrons for a Highly Accelerated Electron Population (Fig. 8b) and Accompanying Ion Conics (Fig. 8a). The dashed ellipse in Fig. 8b corresponds to the 12 keV peak in the electron spectrum while the dashed lines in Fig. 8a separate ionospheric and magnetospheric ions.

previous cases at the peak energy of the precipitating electrons. Nearly constant phase space densities parallel to the v_{\perp} axis inside the inferred ellipse are observed. Another feature is the low velocity electron beams that occur well inside the atmospheric loss cone; these result from the enhanced primary electrons producing secondaries in the ionosphere. Electrostatic reflection of electrons with energies below ~ 12 keV results in a net current flow near zero for $0.17 < E < 12$ keV. Fig. 8a shows well defined ion conical distributions during this time period with peak fluxes near $\sim 130^{\circ}$ pitch angles. The dotted lines in Figs. 8a and 8b represent asymptotes for hyperbolae which separate ionospheric and magnetospherically trapped phase space densities (Croley et al., 1978). The first adiabatic invariant relationship puts the mirror point of these ion conical distributions at $|B| = 0.106$ Gauss, which represents an altitude near 4700 km, some 2700 km below the satellite. One other interesting comparison between these distribution functions and previous ones is the enhanced high frequency waves that occur between ~ 0.3 and 2 kHz in the Fig. 1 spectrogram.

The peak in the precipitating electron spectrum near 8.5 keV for data in Fig. 7b and a peak in the precipitating electron spectrum near 12 keV in Fig. 8b are the only similarities between these two electron distributions. To contrast the shapes of the contours let us examine the following examples: for parallel velocities near $v_{\parallel} = 5.4 \times 10^4$ km/sec,

$$f(v) = 0.018 (\text{sec}^3\text{-km}^{-6}) \text{ in Fig. 7b and } f(v) = 0.49 (\text{sec}^3\text{-km}^{-6}) \text{ in Fig. 8b.}$$

However, for small perpendicular velocities at $v_{\perp} = 1.1 \times 10^4$ km/sec,

$$f(v) = 80 (\text{sec}^3\text{-km}^{-6}) \text{ in Fig. 7b and } f(v) = 4.3 (\text{sec}^3\text{-km}^{-6}) \text{ in Fig. 8b.}$$

This means that for two regions where the potential drop above the satellite is approximately the same, phase-space density ratios for ~ 0.36 keV (1.1×10^4 km/sec) and 8.4 keV (5.4×10^4 km/sec) electrons varied by as much as a factor of 500 when viewed along the v_{\parallel} and v_{\perp} axis. We shall pursue this observation further in the discussion section.

Another interesting comparison between distributions near 40918 and 41229 sec UT are the ion distributions shown in Fig. 8a and Fig. 7a respectively. Conical distributions up to ~ 1 keV are observed in Fig. 8a when the electron distribution functions elongate along the v_{\parallel} axis and low energy (< 100 eV) field-aligned ion distributions are observed in Fig. 7a when the electron iso-distribution function contours elongate along the v_{\perp} axis. Whether or not these electron features are associated on a one-to-one basis with the ions is yet too early to determine; nevertheless, the types of distribution functions observed in Figs. 7b and 8b are rather common observations in the S3-3 data.

Just prior to entering the last acceleration region that extends from ~ 41278 to 41445 sec UT, the strongest electron acceleration signature is encountered. Fig. 9b shows the electron distribution function contours for 41263 to 41285 sec UT. A complete angular rotation is shown because of the changes in the phase space density profiles during the time interval required for 1 satellite rotation. Near 41263 sec UT, the electron spectrometers are sampling fluxes with pitch angles near 0° (i.e., $+v_{\parallel}$) The intensity gradient in the 33 keV electron channel is field aligned and varies approximately two orders of magnitude from $60^{\circ} < \alpha_p < 20^{\circ}$ (A. L. Vampola, private communication, 1979). This should be contrasted with the angular distributions for electrons in Fig. 7b and Sharp et al., 1979 (Fig. 3), where the pitch angle gradients over a comparable angular range (i.e. $\sim 40^{\circ}$) are only around a factor of 2.

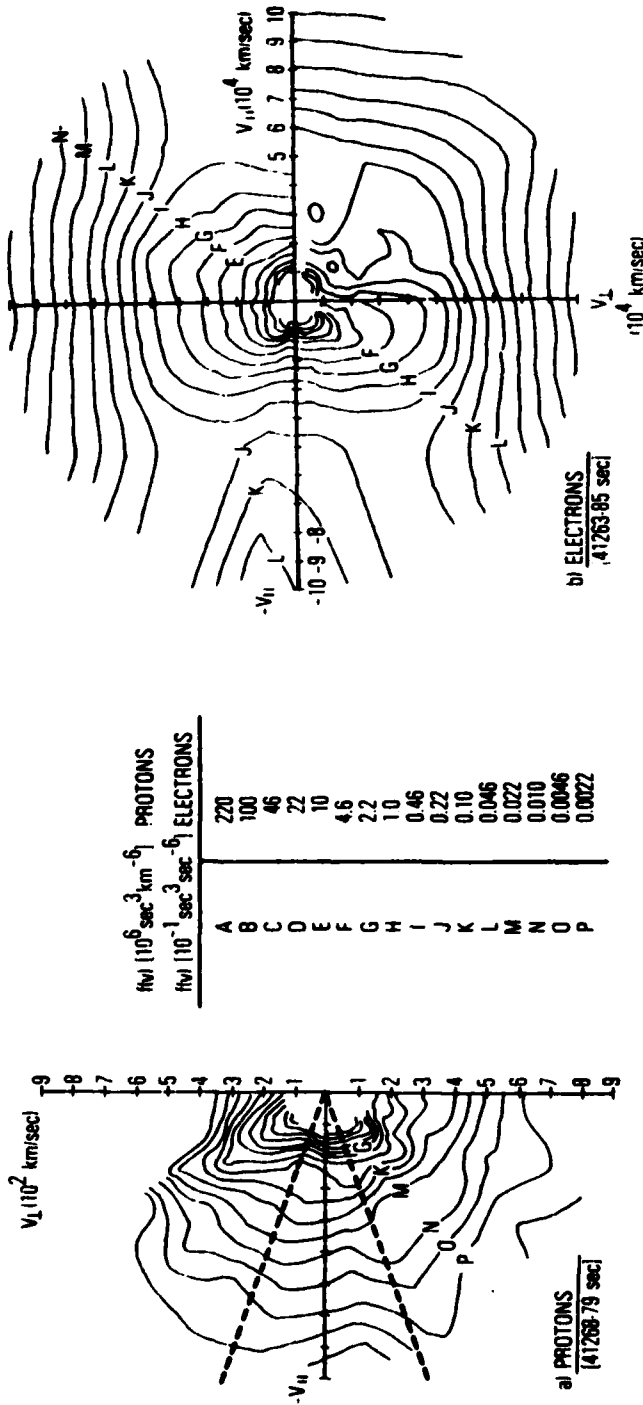


Fig. 9. Ion Phase Space Density Contours in Fig. 9a Showing the Crossing of an Ion Conical Distribution Outside of the Ionospheric Loss Cone (dashed lines). At this same time, electrons are shown to be accelerated up to ~33 keV at the top half of Fig. 9b and then decrease to lower energies during one satellite rotation.

In addition, the peak intensity at the highest energy (33 keV) in Fig. 9b occurs near $15^\circ - 20^\circ$ pitch angle, with a factor of 2 reduction in flux at the closest approach to the magnetic field (within $\sim 7^\circ$). This observation should also be compared with Sharp et al., 1979 (Fig. 3), where the intensity of ~ 10 keV electrons begins to drop for $\alpha_p < 40^\circ$.

In the time required to obtain a complete angular distribution (~ 22 sec), the phase-space density contours at high velocities ($\sim 10 \times 10^4$ km/sec) change from open to closed along the $+v_z$ axis. During this transition time, ion conics are shown in Fig. 9a outside of the atmospheric loss cone indicated by the dashed lines. These highly anisotropic and accelerated electron distributions occur in between regions of strong DC electric fields but are closely related to strong AC electric field signals. In fact, the two strongest broadbanded noise signals observed extend to high frequencies (> 8 kHz) and are spatially associated with these types of electron distributions near 40910 and 40260 sec UT.

The final region of interest occurs just before the satellite crosses onto polar cap field lines. As shown in the compressed data in Fig. 2, the region between 41.28 to 41.42 ksec UT contains very turbulent DC electric fields and numerous strong field structures. Upon entering this region near 41278 sec UT, a strong saturated northwest component of the DC electric field was observed that produced a potential drop along the satellite trajectory approaching 10 kV. The first ion spectrum at 180° was measured at 41295 sec UT and showed maximum intensity for energies above 3.9 keV. Figs. 1 and 2 show a series of ion beams coming up the magnetic field lines. Table I lists the times for observing these upcoming ion beams, an estimate of the energy where the maximum intensity occurs, and the approximate flux intensity. Included in Table I are measurements from the Lockheed ion spectrometer (R. D.

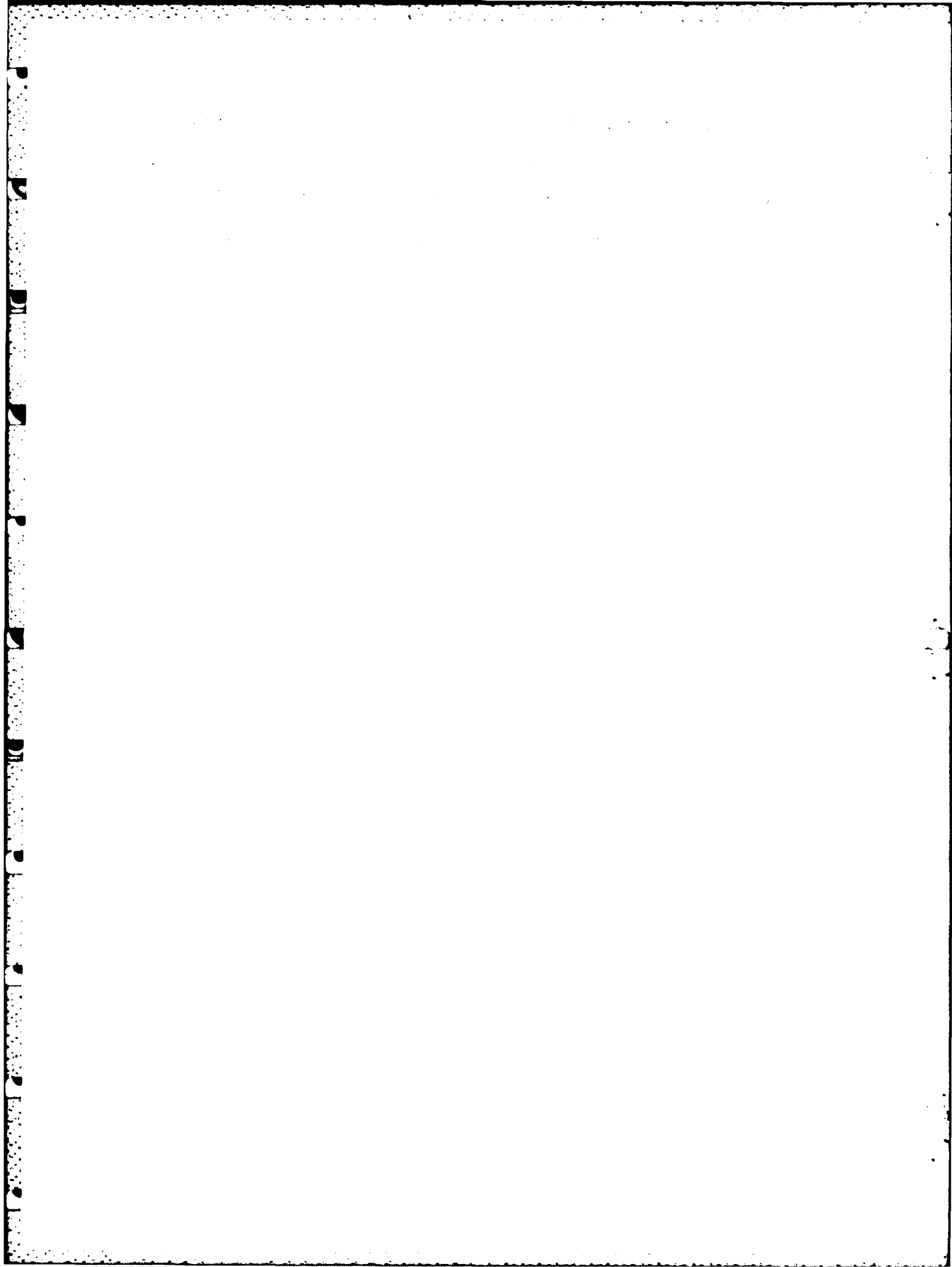
Table 1. Times, Energy at the Peak Intensity, and Intensity of Proton Beams Estimated from Data Taken by the Electrostatic Analyzer, with Energies from 0.09 to 3.9 keV, and the Ion Compositions Spectrometer, with Energies Between 0.5 to 16 keV.* The time interval between 41300 to 41400 sec is a broad region of particles acceleration and electric field variability, as seen in Fig. 2.

<u>UT(SEC)</u>	<u>Spectral Peak (keV)</u>	<u>Flux (cm² -ster-sec-keV)⁻¹</u>
41295	> 3.9	~ 5 x 10 ⁴
41301	> 8.5*	~ 5 x 10 ⁶
41317	~ 2.3	~ 6 x 10 ⁶
41323	~ 3.3*	~ 2 x 10 ⁶
41340	> 3.9	~ 1 x 10 ⁷
41346	~ 1.3*	~ 2 x 10 ⁷
41362	~ 3.1	~ 4 x 10 ⁶
41368	~ 8.5*	~ 8 x 10 ⁶
41384	~ 2.3	~ 4 x 10 ⁶
41390	~ 0.94*	~ 1 x 10 ⁶
41406	> 3.9	~ 2 x 10 ⁶
41412	~ 16*	~ 3 x 10 ⁶
41429	~ 2.3	~ 7 x 10 ⁶

*Lockheed Spectrometer

Sharp, private communication, 1978) that provides a three-point spectrum somewhere between 0.5 and 16 keV and lags the ion ESA measurements by 1/4 spin period or ~ 5.8 sec. Even though the estimates of the peak energy are approximate, there are clear indications that the energies of the ion beams are changing dramatically over this broad spatial region of acceleration. For example, the first two measurements in Table I (41295 and 41301 sec UT) show ion beams with energies approaching 10 keV. The calculated potential drop (from Eq. 1) along the satellite trajectory changed by at least 10 kV in a time interval of ~ 5 sec. Sharp et al., 1979, showed an example of an increased electron loss cone in their Figure 5, from which they estimate a potential drop of ~ 13 kV below S3-3 altitude at this time. Another dramatic change in the ion beam energy occurred between 41362 and 41384 sec UT, when the peak energy changed from ~ 3.1 keV up to ~ 8.5 keV and then down to ~ 2.3 keV. Fig. 2 shows the largest variations of the DC electric field at this time near 41377 (41.38 k) sec UT when the calculated potential (from Eq. 1) increased by ~ 5 kV in a few seconds. Again the electric field signal was saturated. Table I also shows an increase in the ion beam energy between ~ 41390 and 41429 sec UT. Fig. 2 indicates another fluctuation in the DC electric field that occurred near 41397 (41.40 k) sec UT, with a total potential change of only a few kV. There is, therefore, qualitative agreement between increases in ion beam energies and narrow electrostatic enhancements in this region of broad acceleration. Estimates of the potential below the satellite using electron loss cone analysis also confirm this result, although this method is not as sensitive to these changes as are the ion beam data. From Fig. 1, one can see that the precipitating electron distributions are relatively stable and the peak energy remains near 8 keV throughout most of this region. Near 41400 sec UT, the peak electron energy drops down to ~ 5 keV. Sharp et al., 1979 noted the similarity between the accelerated elec-

trons just before and following the strong ~ 33 keV acceleration event described earlier at 41263 sec UT and shown in Fig. 9b. That is, the downgoing electrons are very similar on either side of the strong electron acceleration, which indicates a very broad and relatively stable acceleration region at high altitudes.



Discussion

One of the reasons that the auroral data from the July 29, 1976 acquisition by S3-3 has appeared so frequently is purely circumstantial. More important, however, is that many diverse observations are contained in one auroral pass. While running the risk of suggesting these represent 'typical' data, we feel it is important that these observations are examined in a quantitative fashion. The approach used in the preceding section was to present charged particle distribution functions in the presence of strong electrostatic shocks. Some of these data have been presented by Mozer et al., 1977; Sharp et al., 1979; Cornwall and Schulz, 1979; and Chiu and Cornwall, 1979; and earlier at a special S3-3 AGU session in 1977. One of our primary objectives here is to present the potential derived by directly integrating the perpendicular electric field across narrow enhancements (Eq. 1) and compare that potential with one derived from estimating adiabatic boundaries to the charged particle distributions, since there exists a one-to-one relationship between field reversals and accelerated particles.

If individual shock structures extend far down in altitude and persist for sufficiently long times, then a comparison of potential drops at satellite altitude with potential drops below satellite altitude should yield similar results. Four such examples were considered, and within the experimental uncertainties the two independent methods yield similar results. Experimental problems such as electric field saturation effects, threshold limitations and sensitivity difficulties make this conclusion tentative at best.

In addition to the particle and field comparison, it was shown that field reversals occur simultaneously with the onset of retarded backscattered elec-

trons and near the boundaries of accelerated precipitating electrons. Field reversals can be extremely narrow in latitude and exist individually or occur at the edge of, or inside of, broader regions of acceleration.

Quite distinct from the type of acceleration signature described above are those associated with strong field-aligned gradients in the electron distributions. These field-aligned acceleration signatures are found without local DC electric field enhancements or upcoming ion beams, which suggests that the bulk of the potential drop is above and in close proximity to the measurement. Strong broad-banded noise is associated with these highly anisotropic electrons as well as ion conics. It is tempting to suggest a close relationship between these phenomena. What is clear, however, is that both extended and localized regions of electron acceleration are encountered near the 7000-8000 km altitude near dusk local time. When the potential extends below the satellite altitude, there exists excellent relationship between perpendicular electric fields and acceleration signatures in the charged-particle distributions.

References

- Cattell, C. A., R. L. Lysak, R. B. Torbert and F. S. Mozer, Observations of differences between regions of current flowing into and out of the ionosphere, *Geophys. Res. Lett.* 7, 621, 1979.
- Chiu, Y. T. and M. Schulz, Self-consistent particle and parallel electrostatic field distributions in the magnetospheric-ionospheric auroral region, *J. Geophys. Res.* 83, 629, 1978.
- Chiu, Y. T. and J. M. Cornwall, Electrostatic model of a quiet auroral arc, *J. Geophys. Res.*, 1979.
- Cladis, J. B. and R. D. Sharp, Scale of electric field along magnetic field in an inverted-V event, *J. Geophys. Res.*, 1979.
- Cornwall, J. M. and M. Schulz, Physics of heavy ions in the magnetosphere, *Solar System Plasma Physics*, Vol. III, ed. by L. J. Lanzerotti, C. F. Kennel and E. N. Parker, North-Holland Publishing Co., 1979.
- Croley, Jr., D. R., P. F. Mizera and J. F. Fennell, Signatures of a parallel electric field in ion and electron distributions in velocity space, *J. Geophys. Res.* 83, 2701, 1978.
- Ghielmetti, A. G., R. G. Johnson, R. D. Sharp and E. G. Shelley, The latitudinal diurnal and altitudinal distributions of upward-flowing energetic ions of ionospheric origin, *Geophys. Res. Lett.* 5, 59, 1978.
- Gorney, D., A. Clark, D. Croley, J. Fennell, J. Luhmann and P. Mizera, Auroral ion beam distributions below ~ 8000 km, to be published *J. Geophys. Res.*, 1980.
- Gurnett, D. A. and L. A. Frank, A region of intense plasma turbulence on auroral field lines, *J. Geophys. Res.* 82, 1031, 1977.

- Kaufmann, R. L., P. B. Dusenber, B. J. Thomas and R. L. Arnoldy, Auroral electron distribution functions, *J. Geophys. Res.* 83, 586, 1978.
- Kintner, P. M., M. C. Kelley, R. D. Sharp, A. G. Ghielmetti, M. Temerin, C. Cattell, P. F. Mizera and J. F. Fennell, Simultaneous observations of energetic (keV) upstreaming ions and electrostatic hydrogen cyclotron waves, submitted to *J. Geophys. Res.*, 1979.
- Lysak, R. L., M. K. Hudson and M. Temerin, Ion heating by strong electrostatic ion cyclotron turbulence, *J. Geophys. Res.*, 84, in press, 1979.
- Mizera, P. F. and J. F. Fennell, Signatures of electric fields from high and low altitude particle distributions, *Geophys. Res. Lett.* 4, 311, 1977.
- Mizera, P. F., J. F. Fennell and A. L. Vampola, Charged particle distributions in the presence of large DC electric fields, *EOS* 58, 472, 1977; Correlated charged particle and electron field measurements, *Trans. of the 3rd General Scientific Assembly, IUGG* 41, 166, 1977.
- Mizera, P. F., J. F. Fennell, D. R. Croley, Jr., A. L. Vampola, F. S. Mozer, R. B. Torbert, M. Temerin, R. L. Lysak, M. K. Hudson, C. A. Cattell, R. G. Johnson, R. D. Sharp and A. Ghielmetti, The aurora inferred from S3-3 particles and fields, in press, *J. Geophys. Res.*, 1980.
- Mozer, F. S., C. W. Carlson, M. K. Hudson, R. B. Torbert, B. Paraty, J. Yatteau and M. C. Kelley, Observations of paired electrostatic shocks in the polar magnetosphere, *Phys. Rev. Lett.* 38, 292, 1977.
- Sharp, R. D., R. G. Johnson and E. G. Shelley, Observation of an ionospheric acceleration mechanism producing energetic (keV) ions primarily normal to the geomagnetic field direction, *J. Geophys. Res.* 82, 3324, 1977.
- Sharp, R. D., R. G. Johnson and E. G. Shelley, Energetic particle measurements from within ionospheric structures responsible for auroral acceleration, *J. Geophys. Res.* 84, 480, 1979.

- Shelley, E. G., R. D. Sharp and R. C. Johnson, Satellite observations of an ionospheric acceleration mechanism, *Geophys. Res. Lett.* 3, 654, 1976.
- Temerin, M. A., The polarization, frequency, and wavelengths of high latitude turbulence, *J. Geophys. Res.* 83, 2609, 1978.
- Torbert, R. B. and F. S. Mozer, Electrostatic shocks as the source of discrete auroral arcs, *Geophys. Res. Lett.* 5, 135, 1978.
- Ungstrup, E., D. M. Klumpar and W. J. Heikkila, Heating of ions to supra-thermal energies in the topside ionosphere by electrostatic ion cyclotron waves, *J. Geophys. Res.* 84, 4289, 1979.
- Whipple, E. C., Jr., The signature of parallel electric fields in a collisionless plasma, *J. Geophys. Res.* 82, 1525, 1977.

LABORATORY OPERATIONS

The Laboratory Operations of The Aerospace Corporation is conducting experimental and theoretical investigations necessary for the evaluation and application of scientific advances to new military space systems. Versatility and flexibility have been developed to a high degree by the laboratory personnel in dealing with the many problems encountered in the nation's rapidly developing space systems. Expertise in the latest scientific developments is vital to the accomplishment of tasks related to these problems. The laboratories that contribute to this research are:

Aerophysics Laboratory: Launch vehicle and reentry aerodynamics and heat transfer, propulsion chemistry and fluid mechanics, structural mechanics, flight dynamics; high-temperature thermomechanics, gas kinetics and radiation; research in environmental chemistry and contamination; cw and pulsed chemical laser development including chemical kinetics, spectroscopy, optical resonators and beam pointing, atmospheric propagation, laser effects and countermeasures.

Chemistry and Physics Laboratory: Atmospheric chemical reactions, atmospheric optics, light scattering, state-specific chemical reactions and radiation transport in rocket plumes, applied laser spectroscopy, laser chemistry, battery electrochemistry, space vacuum and radiation effects on materials, lubrication and surface phenomena, thermionic emission, photosensitive materials and detectors, atomic frequency standards, and bioenvironmental research and monitoring.

Electronics Research Laboratory: Microelectronics, GaAs low-noise and power devices, semiconductor lasers, electromagnetic and optical propagation phenomena, quantum electronics, laser communications, lidar, and electro-optics; communication sciences, applied electronics, semiconductor crystal and device physics, radiometric imaging; millimeter-wave and microwave technology.

Information Sciences Research Office: Program verification, program translation, performance-sensitive system design, distributed architectures for spaceborne computers, fault-tolerant computer systems, artificial intelligence, and microelectronics applications.

Materials Sciences Laboratory: Development of new materials: metal matrix composites, polymers, and new forms of carbon; component failure analysis and reliability; fracture mechanics and stress corrosion; evaluation of materials in space environment; materials performance in space transportation systems; analysis of systems vulnerability and survivability in enemy-induced environments.

Space Sciences Laboratory: Atmospheric and ionospheric physics, radiation from the atmosphere, density and composition of the upper atmosphere, aurorae and airglow; magnetospheric physics, cosmic rays, generation and propagation of plasma waves in the magnetosphere; solar physics, infrared astronomy; the effects of nuclear explosions, magnetic storms, and solar activity on the earth's atmosphere, ionosphere, and magnetosphere; the effects of optical, electromagnetic, and particulate radiations in space and space systems.

. . .

END

FILMED